LASER & PHOTONICS REVIEWS
www.lpr-journal.org

Light-adaptive Mimicking Retina with In Situ Image Memorization via Resistive Switching Photomemristor Arrays

*Zijun Hu, Ying Hu, Li Su, and Xiaosheng Fang**

Artificial visual memory systems have been of particular interest since the development of machine vision and bionic robots. Ordinarily, the conventional system architecture requires the complex integration of two functional modules, a photo-sensor and a memory device, which greatly limits the operating efficiency and increases the extra energy consumption. Nonetheless, other simply configured optoelectronics memory devices generally face challenges of adaption in complex light environments. Here, a resistive switching (RS) perovskite-based photomemristor is presented that mimics the retina function. The dual function of light perception and in situ storage are both achieved. In the dark condition, it exhibits impressive memory performance with a high ON/OFF ratio of 10^4, a long retention time of over 10^4 s, and a low operating voltage of 0.38 V. With illumination, it shows self-powered, broadband photo-detecting characteristics with responsivity of 70 mA W^{-1} and detectivity of 7.5×10^{10} Jones. More importantly, benefiting from the material dual-phase configuration, the highly steady photo-adjusted RS windows are achieved. Its light-adaptive memory application in dynamic environments is further demonstrated using the mimicking retina for a machine eye. This work can provide a strategy for enhanced RS photomemristor and its application in changing and varied scenarios.

1. Introduction

Environmental lights are complex and various, which necessitates bio-eyes with self-adaptive capability for light perception,[1,2] and for the subsequent image memorization process in the brain cortex. Therefore, vision adaption and memory are the main challenges in developing artificial vision systems. Nowadays, diverse structure layouts have been widely explored.[3–6] While conventional complicated hardware assembling owns the disadvantages of large power consumption among modules. And the Moore's law is bringing the integration bottle toward all advanced electronic devices. Therefore, to develop optoelectronic memory devices in simplified frames would meet the new trends in the advanced artificial visual system.[7–9]

Memristor, benefiting from the two-terminal simple structure and generally lower power consumption than transistor, has been widely researched. Compared to an ordinary memristor, the photomemristor, with an additive light responsiveness, has been of great interest in vision applications. Normally, the memristor could be divided into two types, the analog memristor and the digital type, according to their resistance tuning pattern. The digital one, also named as resistive switching (RS) memristor, features its binary state storage of 0/1, could offer high storage precision and stable controllability, as well as a long retention time for stable data preservation. While few works have explored the RS photomemristor in building vision systems due to their worse photo-tuning ability by contrast to the analog type. Because for the latter case, the gradual resistance tuning mechanism under photo-electrical signals could well imitate the synaptic neurons. Nonetheless, this type of memristor also suffers from disadvantages, including larger fluctuation in resistance states and low reliability in repeated signals treated. Especially in some strict demanding applications, the digital memristor generally offers more reliable resistance state distinguishment due to the switching operation with a large ON/OFF ratio. Therefore, developing the RS memristor with steady photoelectric coupling performance is a highly demanded issue. Recently, many reported RS photomemristors have exhibited complex and deteriorated light-controlled effects.[10–12] For example, the memristive windows would become extremely unstable or collapse under light stimuli.[13–16] Such poor photoelectrical behavior obviously restricts their further employment in retinal mimicking applications. It still remains a considerable challenge in performance optimization from both material and device configuration.

Currently, diverse material media have been explored, such as photosensitive 2D material,[17,18] selenide semiconductors,[4,5] and halide perovskites (PVK).[1,19,20] Among them, organic–inorganic hybrid perovskite (OIHP) materials with ABX_3 structures are famously applied in opto-electrical devices

Z. Hu, Y. Hu, L. Su, X. Fang
Department of Materials Science
State Key Laboratory of Molecular Engineering of Polymers Fudan University
Shanghai 200433, P. R. China
E-mail: xshfang@fudan.edu.cn

The ORCID identification number(s) for the author(s) of this article can be found under https://doi.org/10.1002/lpor.202301364

DOI: 10.1002/lpor.202301364

due to their advantages of superior light absorption and conversion efficiency.[21–23] Also, because of their innate hysteresis and innumerable charge/ion transport channels, these materials have been explored in memory devices, such as $MAPbX_3$ (X = Cl, Br, I) and $FAPbI_3$ based robust memristors.[24–26] Therefore, these OIHP-based media give a good material choice for a high-performance RS photomemristor. For example, a halide perovskite-based photomemristor of $Au/CH_3NH_3PbI_{3-x}Cl_x/FTO$ was introduced.[27] With irradiation of varied power intensity applied to the device, the RS memory window exhibited light density-dependent behaviors with the maximum V_{SET} value of 1.47 V (dark) reducing to 0.1 V when density increased. For the light wavelength-dependent RS memristor, the V_{SET} value could be modulated from 0.9 to 0.3 V, enabling the possibility of three-color recognition and artificial retina system construction.[28] Although light-controlled storage behaviors were achieved in these works, only a few light conditions and their induced resistances were clearly demonstrated and distinguished. The very limited light modulation room, which is based on the maximum V_{SET} under dark condition, has greatly restrained them for visual application. Therefore, it is essential to explore other effective approaches to achieve a more accurate and larger light-tuning room of multiple resistances in RS memristors. In this work, the unique dual-phase structure of the material has effectively solved these problems. The perovskite was mainly composed of photosensitive α phase and insensitive δ phase. The photo-inactive δ phase guaranteed the stable memristive switching process without light facilitating effect to shift V_{SET}. And the photoactive α phase ensured the photo-adjustable resistance states. As a result, a stable and large photo-tuning resistance modulation room was realized. Therefore, this mechanism offered a new insight in developing an enhanced multifunctional resistive switching optically controlled memristor.

In this study, we construct an RS photomemristor array based on the OIHP-film of $Cs_xFA_yMA_{1-y-x}Pb(I_zBr_{1-z})_3$ (denoted as CFMPBI) for retinal mimicking. The dual function of storage and photodetecting was individually achieved in the structure of Cu/CFMPBI/Au. For light perception, a self-powered responsivity of 70 mA W^{-1} and detectivity of 7.5×10^{10} Jones was realized, with an ability to detect the environmental light density weak as 1.5 μW cm^{-2}. For the nonvolatile storage, the Cu/PVK/Au exhibited excellent performance with a large ON/OFF ratio ($\approx 10^4$), and long retention time ($>10^4$ s), as well as the in situ image memorization. Moreover, its stable photo-tuning electrical switching memory behavior was demonstrated for the first time under broadband irradiation, suggesting the self-adaptive ability in various scenarios. This work could encourage the advancement of RS-based photomemristors and applications in machine vision systems.

2. Results and Discussion

Bio-visual system mainly consists of retina, optic nerves, and visual cortex (**Figure 1a**). The retina plays an important role in visual adaptation, which allows eyes to adjust photoresponse according to varied environment light conditions. Cone and rod cells as photoreceptors in the healthy retina are responsible for light signals sensing and conversion, where cones are mainly responsible for photopic vision and rods are in charge of scotopic. Thus, the retina could function effectively across a wide range of visible light conditions from dim to strong light stimuli. Nowadays, mimicking vision applications have been developed and utilized in artificial intelligence, bio-robot, and medical retina implants for patients with vision disease.[29–31] Therefore, a mimicking retina is supposed to achieve environmental-adaptive imaging in the artificial vision system.

As shown in Figure 1a, we designed a bio-inspired photomemristor array to simulate the retina function, which could operate in dual-mode as a photodetector or a memristor. As a consequence, the dual-function of photo-sensing and storage could be well integrated and working cooperatively in this mimicking retina (Figure 1b). Specifically, to demonstrate the imitation, a 3 × 3 pixel array was investigated for the adaptive-sensing and after-sensing memory. As the letter H shape mask induced light stimuli were applied to the device array under a series of diminishing optical conditions down to 0 μW cm^{-2} (Figure 1c), the photocurrent response was collected and mapped proportional to the color shade. The results exhibited a notably adaptive behavior as brightness. Correspondingly, after removing the external exposure, the image "H" could be electrically memorized as shown in the encoded pixels (Figure 1d). Each pixel has the storage binary states of 0/1 representing the high/low resistance state (HRS/LRS) of a memristor. With certain electrical stimulation ($V > V_{SET}$) applied to pixels marked as "1" (Figure 1d Left), the "H" pattern could be in-situ memorized as intended. As a result, the two processes could well imitate the retina operation scenarios with and without illumination. In human eye blink cycle, the mimicking retina could achieve light-adaptive image sensing when eyes open (illumination state), and in-situ memorization in the same pixels after eye closed (dark state).

Figure 2a shows the schematic device array configuration based on the perovskite film. For each pixel, the photomemristor exhibits a sandwiched structure of $Cu/Cs_xFA_yMA_{1-x-y}Pb(I_zBr_{1-z})_3/Au$. The corresponding optical images are shown in Figure S1 (Supporting Information) with dense and uniform quality. In Figure 2b, the clear and close-packed PVK grains with an average size of 300–500 nm could be observed in the top-view SEM image. The cross-section SEM image below indicates the film with an even thickness of less than 500 nm and without a significant pinhole inside. Specifically, the uniform film surface presents a small roughness of 37 nm over the area of 5 μm × 5 μm by atomic force microscopy (AFM) (Figure 2c). The highly homogeneous morphology (Figure S1c,d, Supporting Information) ensures the middle layer with good contact with the pair electrodes of Au and Cu, which is beneficial for improving device performance and uniformity.

The Grazing Incidence Wide-Angle X-ray Scattering (GIWAXS) result (Figure S2, Supporting Information) and X-ray diffraction (XRD) spectra (Figure 2d) were characterized for the $Cs_xFA_yMA_{1-x-y}Pb(I_zBr_{1-z})_3$ film. The triple-cation mixed-halide perovskite derived from organo-lead compound of $APbX_3$, where A represents an organic cation such as MA^+ (methylammonium), FA^+ (formamidinium) and X stands for halide anion (e.g., I, Br, Cl). It is reported that mixing organic FA, MA, and inorganic Cs cations on the A site is beneficial for the optoelectrical efficiency and environmental stability improvement.[32] Replacing partial I^- with Br^- would further lead to a wide tunable

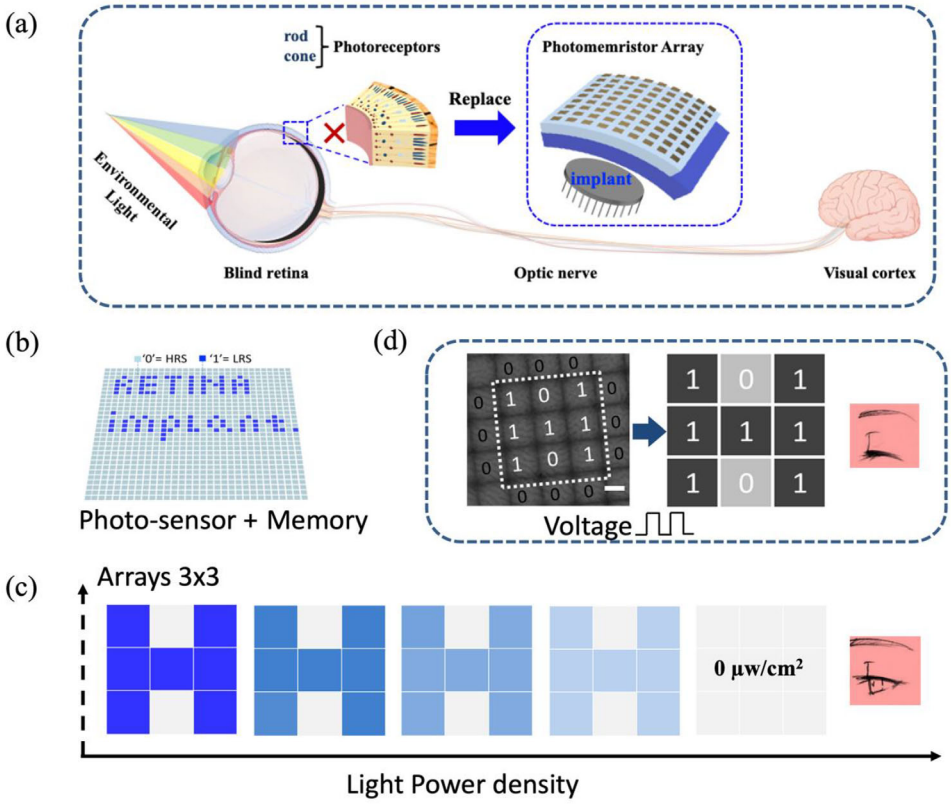

Figure 1. Schematic illustration of the dual-mode photomemristor arrays including perception and in-situ memorization. a) Schematic diagram of the biologic visual system with disabled retina and the functional mimicking retina device. Cones and rods as photoreceptor cells in blind retina unable to convert light signals to electrical ones, which normally deliver through optic nerves to the final visual cortex. Inset: Schematic of photomemristor arrays with a vertical stack structure of Cu/perovskite/Au for each pixel device. b) Schematic concept of photomemristor arrays as image pixels for photo-sensing and in-situ memorization function. HRS/LRS are short for high/low resistance states in each memristor, normally marked as 0/1 in binary storage. c) Left: Scanning electron microscopy (SEM) image of the perovskite film with Au electrode arrays, scale bar: 50 μm. Right: binary image according to the encoded results. d) Schematic of the contrast results of adaptive photo imaging of "H" shape on 3 × 3 array under different light density stimuli.

band gap.[33] Given these strategies, the CFMPBI film, although with complex composition,[34] demonstrates great performance and structural stability, which is essential and preferable for establishing multifunctional devices operated under coupled onto-electrical signals. In Figure 2d, the strongest representative diffraction peak of δ-phase perovskite (11.4°) was found in the film, indicating the photoinactive δ-$FAPbI_3$ as the main phase,[35–37] which plays a vital role in structure stability as well as good memristive behavior.[37–39] Three other typical peaks at 2θ of 14.1°, 28.4°, and 32.1° were also found, which are respectively attributed to the (100), (200), and (210) crystal planes of α-phase FA-based perovskite,[32] and the doping ratio of other ions would only cause a small shift in these peaks position.[40] Contrary to the δ-phase, this photoactive α-phase in CFMPBI mainly contributed to the remarkable photoresponsivity. Besides, the peak at 12.6° attributed to the (001) plane of the impurity PbI_2, the small excess of PbI_2 could passivate the perovskite film for enhanced stability.[32] In addition, the chemical composition and the valance states of the constituting element in the perovskite were analyzed by X-ray photoelectron spectra (XPS) in Figure 2e. The main peaks of Cs 3d, Pb 4f, Br 3d, and I 3d were identified in survey spectra, indicating that element Cs has been successfully doped in the mixed cations. The high-resolution XPS elements results are displayed in Figure S3 (Supporting Information) in detail. These spectra' shape and position are in accordance with a previous report for triple cation mixed perovskite. The above structural characterizations show that we have successfully prepared the CFMPBI film with good quality. Furthermore, to investigate the bandgap structure of the PVK film, both absorption and photoluminescence (PL) spectra were characterized. The Tauc-plot of $(ah\nu)^2$ versus photon energy ($h\nu$) was extracted from the absorption plot to acquire the energy gap as 1.64 eV (Figure 2f), showing an excellent agreement with the PL result of 750 nm peak (Figure S4, Supporting Information). This relatively small bandgap has enabled the PVK film-based retinal mimicking device with a wide light perception range from visible (VIS) to ultraviolet (UV).

To investigate the memristor performance of the Cu/CFMPBI/Au, a typical I–V dual sweep was consecutively performed from −1.0 V to 1.0 V as shown in **Figure 3a**, the memory window demonstrated superior stability and consistency for 40 cycles. Within one cycle, as the applied voltage increases over the threshold voltage (V_{th}, also as V_{SET}) of ≈± 0.38 V, the HRS turns

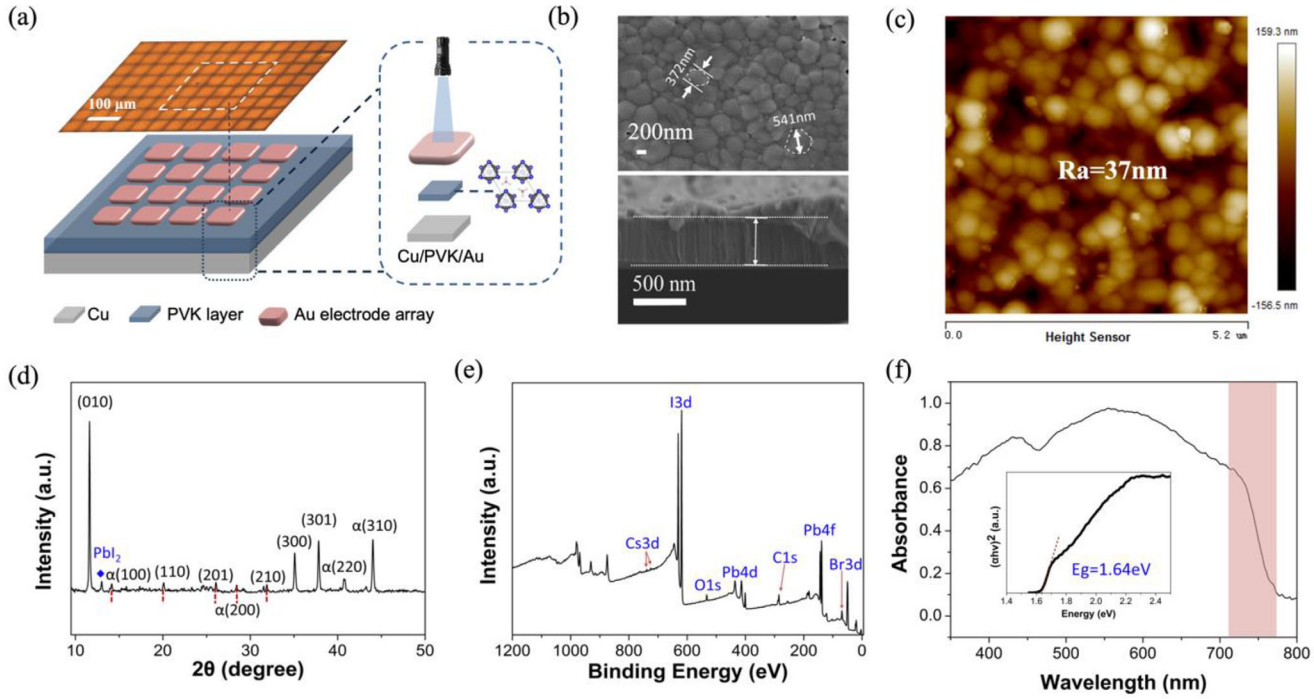

Figure 2. The structural characterization of the $Cs_xFA_yMA_{1-x-y}Pb(I_zBr_{1-z})_3$ active layer. a) Schematic of the device structure of Cu/CFMPBI/Au array. The optical image above indicates the top electrode area of 50 μm × 50 μm per pixel. Inset: diagram of a single device under illumination with a vertical two-terminal structure. b) Top: plane-view of high-resolution scanning electron microscopy (SEM) image of the CFMPBI film. Bottom: the cross-section of the SEM image of the film. c) AFM image of the CFMPBI film with average roughness Ra of 37 nm for 5 μm × 5 μm area. d) XRD spectra of the CFMPBI film. e) XPS survey result of the CFMPBI film. f) Absorbance curve and (inset) the Tauc-plot for the measured optical bandgap of CFMPBI.

to LRS with a low power consumption of ≈100 pW ($P_{SET} = V_{SET} \times I_{SET}$). Inversely, when the voltage drops below the hold voltage (V_{hold}), the LRS switches back to HRS. As a result, the large ON/OFF ratio of ≈10^4 under current compliance (I_{CC}) of 10 μA is acquired. Besides, the bidirectional symmetric RS behavior under three other I_{CC} of 1, 100, and 1000 μA are displayed in Figure S5 (Supporting Information), indicating that multilevel resistance states could be achieved in one unit device with multiple data storage capacity, which is of great significance in storage density enhancement. To evaluate the uniformity of V_{th} among cell devices, the cumulative probability of thirty random cells was statistically analyzed (Figure S6, Supporting Information). Actually, the values of V_{SET} and ON/OFF ratio are significantly influenced by the device area, which are further explored in Figure S17 (Supporting Information). These results show great performance uniformity of the device array. In addition, to assess the device reliability and stability, the endurance test was performed over a 5 × 5 device array (Figure S20, Supporting Information), and an average endurance of ≈300 cycles was obtained for the Cu/CFMPBI/Au. Besides, a long-term retention over 10^4 s was realized under a read voltage of 0.05 V (Figure 3b), the inset shows the device structure under test. Notably, an unstable declining trend of LRS appeared after 1000 s. We believe this slight fluctuation is attributed to the stability change of the conductive filaments between the pair electrodes. Specifically, the metallic Cu and iodine vacancy defects constituted the main components in the conducting bridge across the PVK, where the Cu atoms originated from the active electrode Cu after a process of electrochemical metallization (ECM). As the filaments existed for a period of time, the ion's migration would inevitably lead to the local instability of the conductive paths, which was a very common symptom till the ultimate rupture.

To understand the *I*–*V* switching mechanism, the log (*I*) vs log (*V*) from *I*–*V* curve was fitted as shown in Figure 3c, which could be divided into two stages as HRS and LRS. For the LRS stage, the linear fitting slope of ≈1 corresponds to the Ohmic law, suggesting the successful formation of highly conductive filaments between the top and bottom electrodes. As schematically displayed in Figure 3d, when the positive voltage on Cu exceeds the V_{SET}, the Cu atoms and I^- vacancies/interstitials accumulate to bridge as conducting filaments. While a reverse voltage direction would result in filaments rupture and reset to the HRS (Figure 3e). The conducting mechanism in this stage follows the linear fitting result of $\mathrm{Ln}(I/V) \sim \sqrt{V}$ (Figure 3c), which corresponds to the Schottky contact. To confirm this, the contact interface and band structure of CFMPBI were analyzed in detail (Figure S7a–d, Supporting Information). Since the work function of Au and Cu electrodes are 5.10 eV and 4.65 eV respectively, which are both higher than that of CFMPBI. After the sandwiched structure was built, the Schottky barrier would form at both interfaces between PVK and pair electrodes with calculated 1.7 eV for Cu and 2.15 eV for Au as Figure 3e (Left) shows. The asymmetric Schottky barrier height would lead to a net build-in contact potential of 0.45 eV in the device with an orientation from Cu to Au, marked as $E_{Cu/Au}$. Therefore, the initial HRS stage is consistent with the Schottky mechanism. Furthermore, under the illumination condition, substantial photoinduced electron-hole pairs were generated in Figure 3e (Right). These carriers could

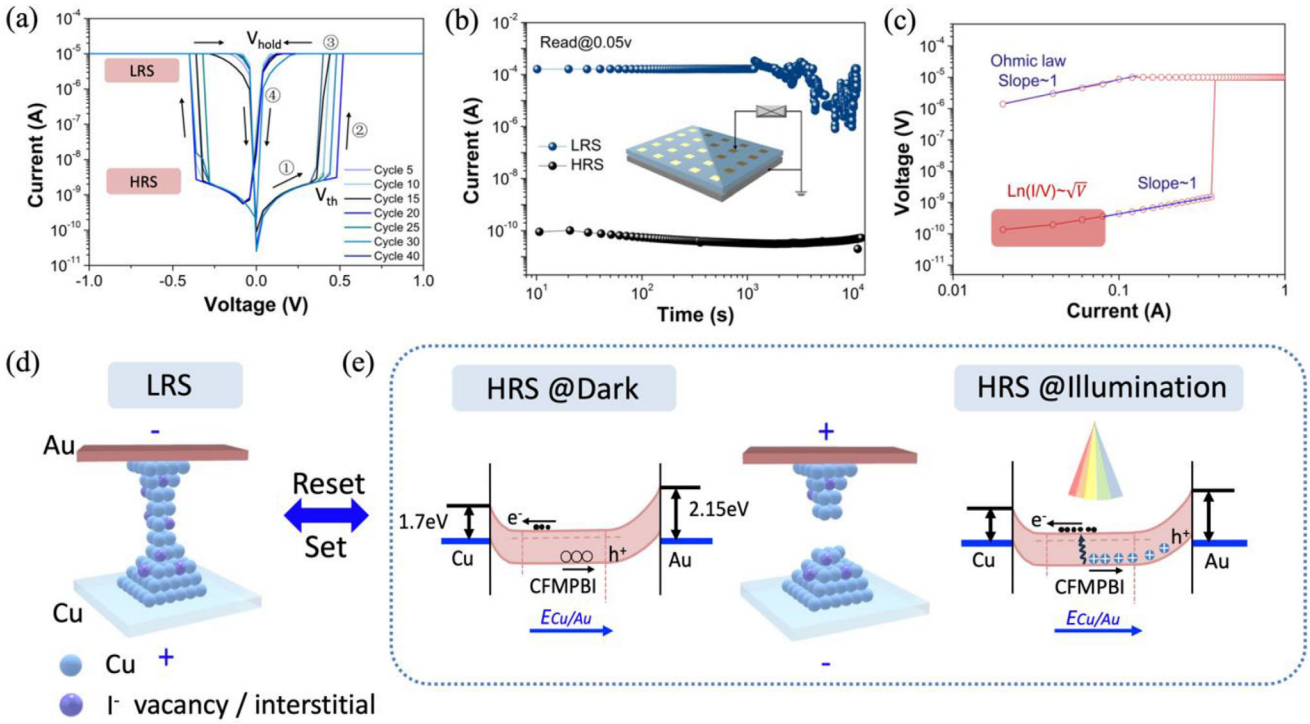

Figure 3. The nonvolatile storage performance of the Cu/CFMPBI/Au. **a)** I-V characteristics of the Cu/CFMPBI/Au for reproducible 40 cycles under the Icc of 10 μA with a sweeping route of −1.0 V→0 V→+1 V→0 V→−1.0 V on the dark status. b) Characterization of data retention time ('0' and '1') at V_{read} of 0.05 V. Inset: the schematic diagram of test device structure with Au electrode area of 120 μm × 120 μm per device for the measurements. c) Log (I) versus log (V) from the typical I-V curve in a. d) Schematic of LRS ($V > V_{th}$) during the resistive switching operation process with conducting fiber bridging pair electrodes. e) Schematic of HRS with energy band diagram illustration of Cu/PVK/Au structure under dark conditions and illumination status.

be separated by this internal electric field with electrons flowing to Cu and holes to Au without external voltage. As a result, the high-resistance values could be effectively tuned by controlling light conditions, depending on the intensity and wavelength. This gives an important foundation for the implementation of photo-tunable applications in our mimicking retina.

The optoelectronic performance of Cu/CFMPBI/Au is characterized in **Figure 4**. By controlling the applied voltage within the V_{SET} range, the device could function as a photodetector. Figure 4a shows the *I–V* characteristics from −0.3 V to 0.3 V under 470 nm with different power densities. Benefiting from the asymmetric electrode collocation as well as the photoresponse, the self-powered photocurrent demonstrates a clear positive correlation with brightness, with the 0 V value around 10^{-8} A at the largest 2.0 mW cm^{-2}. Specifically in the curve, as the forward positive voltage is applied to the Cu, the photocurrent maintains increasing due to the $E_{Cu/Au}$ direction being consistent with the external electric field. In contrast, under negative voltage, the current initially decreases and then increases due to the internal electric field offset effect. Furthermore, we have evaluated the self-powered responsivity and detectivity under a broad range of wavelength as shown in Figure 4b. The responsivity R and detectivity D* respectively represent the optical response efficiency and weak signals detecting ability from a noisy environment. ($R = (I_{ph} - I_d)/P_{in}S$, where I_{ph} and I_d are the detected currents with and without illumination, respectively. P_{in} is the incident optical power density, and S is the illumination area, and $D^* = R/(2eI_d/S)^{1/2}$, e = 1.6×10^{-19} C). The highest responsivity of 70 mA W^{-1} was obtained at 470 nm as well as the largest detectivity ability of 7.5×10^{10} Jones. The corresponding time-dependent (*I–t*) photoresponse at 0 V bias is shown in Figure 4c, demonstrating clear on-off transitions when light switches and remaining stable during illumination. Additionally, the excellent 0 V behaviors under other wavelengths of 450, 365, and 660 nm were also investigated (Figures S8–S11, Supporting Information).

Subsequently, to evaluate the light adaptation ability in Cu/CFMPBI/Au, the 470 nm illumination with varied power density was applied to the device from 1.2 mW cm^{-2} to weak 1.5 μW cm^{-2}. As shown in Figure 4d (below), light on/off was repeated for cycles at each density, an obvious decreasing trend of photocurrent was observed as density decreased. And the clear current on–off could be observed under 0 V at a given density minimum of 1.5 μW cm^{-2}, indicating the excellent detectivity of the device. For some representative cases as marked, the repeated collected current values were 6.8 nA (1.2 mW cm^{-2}), 4.2 nA (0.95 mW cm^{-2}), 1.8 nA (0.55 mW cm^{-2}), 1.2 nA (0.3 mW cm^{-2}), and 0.22 nA (50 μW cm^{-2}), suggesting a stable perception ability of our retina mimicking device. Furthermore, a 3 × 3 device array was investigated with the light exposure through the pattern "H" mask (refer to Figure S12, Supporting Information). The photocurrents were collected by pixels in Table S1 (Supporting Information) under the above five particular light conditions, and mapped into varied grey levels based on the values (Figure 4d). As a result, the "H" image under

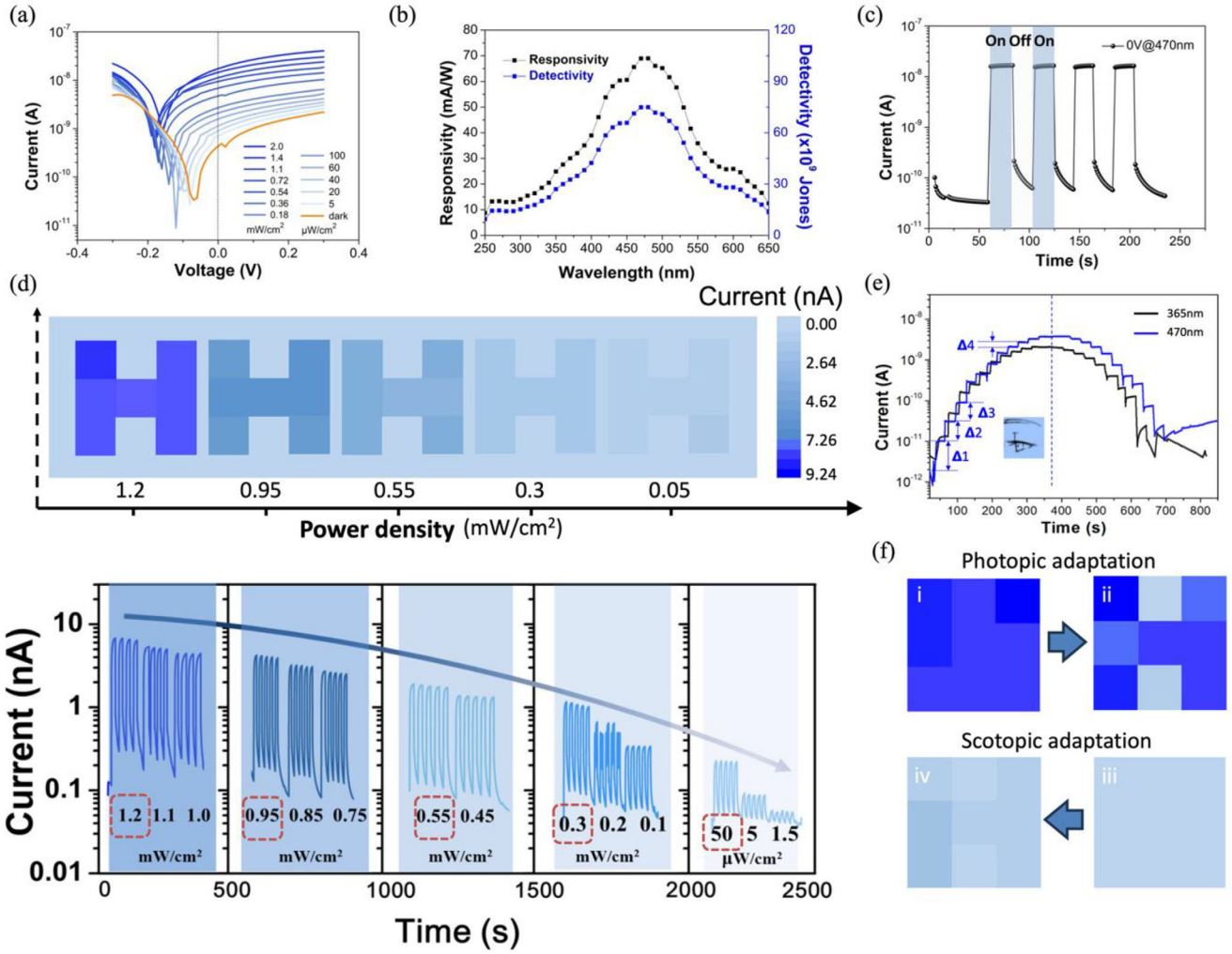

Figure 4. Environmental adaptive image sensing process. a) The *I–V* curves of Cu/PVK/Au under −0.3 V to 0.3 V with a varied light power density (470 nm). b) Responsivity and detectivity of the Cu/PVK/Au. c) The *I–t* curve under 0 V with light switches on/off every 20 s (470 nm 2.0 mW cm^{-2}). d) Bottom: *I–t* characterization with gradient light density irradiation by 20 s on/off. Top: Light-density-dependent image results of 'H' pattern irradiated by specific illuminance from the bottom graph (1.2, 0.95, 0.55, 0.3 mW cm^{-2}, and 50 μW cm^{-2}). e) Mimicking the visual adaptation process from weak light to bright light stimuli in a stepwise increment and reversely. Monochromatic Light used: 365 and 470 nm. f) Schematic of the photopic (top) and scotopic adaptation (bottom) process, the color shade scale is shared with the previous in (d). All the photocurrent measurements above are carried out under zero bias voltage.

higher density conditions would be more clearly discriminated with enhanced image contrast, especially compared to the dim condition of 0.05 mW cm^{-2}, which is analog to human vision with clearer eyesight in a brighter environment.

The environmental lights vary and fluctuate, for instance, from weak to brighter conditions or the reverse process. To imitate this scenario, the 470 nm light was applied to the Cu/PVK/Au device with a step-increased density change then held and reversed. As the light density increases from weak to strong status (Figure S18, Supporting Information). The photocurrent in Figure 4e also exhibits an increasing trend with a decreasing degree. For example, the step density amplitudes of δ_1 (1.5 μW cm^{-2}) < δ_2 (45 μW cm^{-2}) < δ_3 (50 μW cm^{-2}) < δ_4 (180 μW cm^{-2}) in Figure S18a (Supporting Information), result in the photocurrent change in Figure 4e with an obvious relationship of Δ1 > Δ2 > Δ3 > Δ4. Especially, from dark to 1.5 μW cm^{-2}, the minimum δ_1 corresponds to the maximum photocurrent increment of Δ1. While the large increment of δ_4 under a relatively strong light status leads to a much less sensitive photo-response of Δ4. Given this, the process is in accordance with the bio-eyes as they are much more sensitive in dim environments, and try as much as possible to increase photoresponse. While in strong light conditions, as the density increases, the eyes tend to diminish the excess light exposure out of protection. Such self-adaptive behavior to light ensures the ability to cope with dynamic ambient environments. Moreover, this mimicking process was further confirmed with 365 nm wavelength in Figure 4e, also under self-powered mode.

Biologically, the photopic and scotopic adaptation refer to the adaptation to bright and weak light, respectively achieved by cone cells and rod cells in the retina. Inspired by this, our mimicking retina device has demonstrated its adaptive imaging

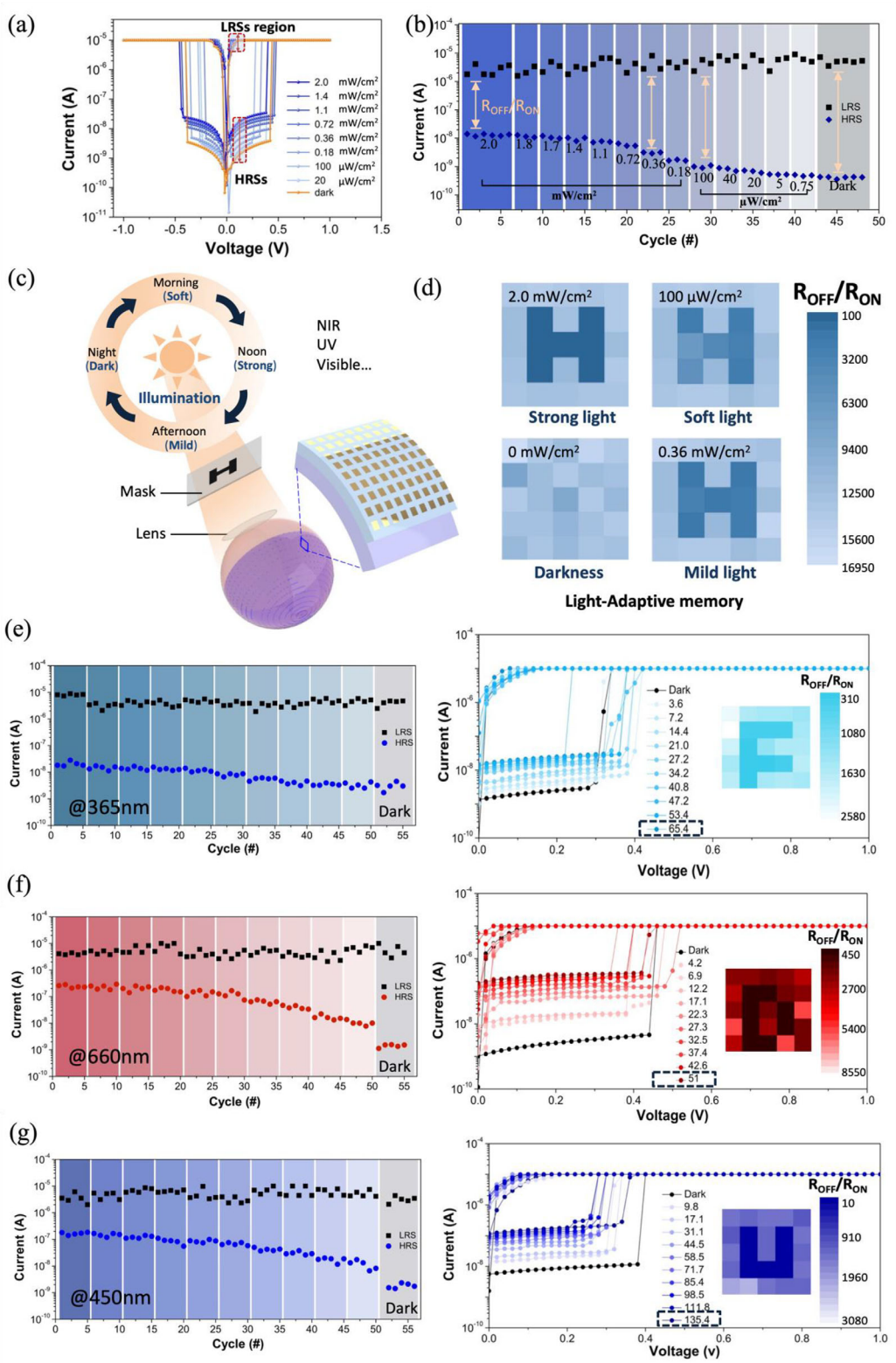

Figure 5. Environmental-adaptive memory behavior. a) Photo-tunable *I–V* switching curves of photomemristor Cu/CFMPBI/Au under various light power densities of 470 nm illumination, dual sweep from −1.0 V to 1.0 V. b) Statistics distribution of HRSs and LRSs values differentiated with varying background color shades based on the light strength, the specific illuminance values marked as 2.0, 1.8, 1.7, 1.4, 1.1, 0.72, 0.36, 0.18 mW cm^{-2} and 100, 40, 20, 5, 0.75 μW cm^{-2}. c) Schematic illustration of the mimicking retina applied in machine eye and operated in diverse environment with various light wavelengths and intensities. The hollow mask is arranged between the light source and the lens of the machine eyeball to image the

ability under the two scenarios. The results are presented in Figure 4f. In the case of photopic adaptation, a strong light of 1.2 mWcm^{-2} was applied to all 3 × 3 pixels, presenting a bright background (Figure 4f-i). Then, an "H" pattern hollow mask was placed above the array (Experimental setup, see Figure S12, Supporting Information), the blocked pixels experienced a notable photocurrent decrease. All the photocurrents of the 3 × 3 device array of Cu/CFMPBI/Au were collected by pixels at 0 V (Table S2, Supporting Information). As a result, the H pattern was successfully imaged with clear contrast (Figure 4f-ii). Similarly, for the scotopic case, the ambient 50 μW cm^{-2} light irradiation presented a weak initial background (Figure 4f-iii). Then mild light of 0.3 mW cm^{-2} exposure was applied to the mask likewise. The exposed pixels exhibited enhanced photocurrents than before, showing great scotopic imaging capability (Figure 4f-iv). Overall, the photopic and scotopic light-adaptive imaging was successfully displayed and well simulated the retina function. Therefore, our mimicking retina device owns superior light-adaptive ability in dynamic light environments. Especially compared to some reported opto-sensor devices with the photocurrent surged behavior under each stimulus, which normally takes several seconds to stabilize,[5,41] our device could adapt to ever-shifting light conditions. Besides, the self-powered, broadband perception combined with the excellent RS memory performance indicate the Cu/CFMPBI/Au as a promising mimicking retina device for future advanced artificial visual systems.

To fully combine and utilize the dual function of sensing and storage, the memory performance under lights was further investigated. **Figure 5a** demonstrates the *I–V* memory windows of Cu/CFMPBI/Au under 470 nm, the largest one corresponds to the dark condition. As the illumination density increases, the RS window exhibits a steady light-adjusted decreasing tendency, this result can be consistently repeated with good stability (Figure S8, Supporting Information). Furthermore, the HRSs and LRSs under a read voltage of 0.05 V were collected under a sequence of light power density (Figure 5b), which ranges from 2.0 mWcm^{-2} to darkness. The maximum brightness and bottom status were repeated for five cycles for HRS/LRS extraction, and three cycles for each rest light condition. To more effectively evaluate the light impacts on variations of both HRSs and LRSs, the ON/OFF ratio (also as R_{OFF}/R_{ON}) was calculated from these statistical results. As the light density decreases, the R_{OFF}/R_{ON} exhibits a gradual expanding trend with the largest 1.3×10^4 for the darkness status and the minimum 2.1×10^2 for the 2.0 mW cm^{-2}. Figure S13 (Supporting Information) presents the overall relationship between the R_{OFF}/R_{ON} and light density, based on which, the lighting conditions on pixels could be inferred by experimental acquired R_{OFF}/R_{ON}. Also, by mapping these values, the information embedded in varying lights could be reproduced.

For a more straightforward application scenario, the mimicking retina is applied on the machine eye in a day routine (Figure 5c). The sunlight brightness follows a cyclic dynamic change: In the morning, the light is weak and gradually increases as the day progresses, then reaches to peak around midday. After noon, the intensity gradually decreases to mild till the evening, the light weakens significantly to darkness. To demonstrate the light-adaptive memory behavior of our mimicking retina throughout a day, we employed a shadow mask between the light source and retina. The performance uniformity among the devices was afore-confirmed for the following exposure of "H" (Figure S21, Supporting Information). As light penetrated through the hallow mask to the photomemristor arrays, the R_{OFF}/R_{ON} values were collected from the 5 × 5 device array and reimaged into color contrast map, as compared in Figure 5d. Specifically, with the strongest 2.0 mWcm^{-2} presenting for the noon condition, the highest contrast of image H was obtained. Because the light-exposed pixels and blocked pixels were respectively presented with the maximum and the minimum level of R_{OFF}/R_{ON} value. While a soft light of 100 μW cm^{-2} leads to the lowest contrast. The mild 0.36 mW cm^{-2} leads to a middle contrast presenting for the afternoon. As for the darkness condition, almost no image was observed among pixels of 5 × 5 array. All the raw data of R_{OFF}/R_{ON} values above were collected in Table S3 (Supporting Information). As a result, the image H exhibits various contrasts in the mimicking retina according to the changed daylight, showing great light-adaptive memory behavior. This demonstrates a good potential for application in dynamic light environment.

Furthermore, the light-adaptive memory behaviors under several other wavelength scenarios were further explored as shown in Figure 5e-g. Likewise, the mask of F, D, and U patterns were respectively applied over the 5 × 5 array under the inducing light of 365, 660, and 450 nm LED with the sequence of tunable brightness. Then, the HRSs and LRSs values were respectively collected each five cycles per density, and statistically compared as shown in the left graph of Figure 5e–g. The 660 nm group of red light would be taken for detailed illustration (Figure 5f). As the intensity-dependent *I–V* memory window is shown on the right, an obviously enlarging window is observed as the light intensity steadily weakens. The light-adaptive R_{OFF}/R_{ON} value reaches to the maximum at a dark state and minimum at the brightest 51.0 mW cm^{-2} (Figure 5f left), well illustrating the phototunable multi-resistances capability in a RS memristor. Accordingly, the 51.0 mWcm^{-2} exposed image "D" exhibited strong contrast due to the smallest R_{OFF}/R_{ON} level in the pattern pixels compared to the background pixels (Table S4, Supporting Information). Also, the brightest conditions of 65 mW cm^{-2} (365 nm) and 135.4 mW cm^{-2} (450 nm) were conducted for letters "F" (Figure 5e) and "U" (Figure 5g), respectively with great image clarity. Besides, the white light tuning results are supplemented in Figures S14 and S15 (Supporting Information). Therefore, with broadband response, our RS photomemristor of

corresponding pattern on the mimicking retina. d) Light-adaptive image memory results of letter "H" pattern by varying 470 nm light intensities as 2.0 mW cm^{-2}, 0.36 mW cm^{-2}, 50 μW cm^{-2}, and darkness. e–g) Light-adaptive image memory behaviors under 365, 660, and 450 nm LED, respectively. The illuminance density values are listed in the corresponding *I–V* curves. Insets: the light-adaptive image results of patterns "F", "D", and "U", which are irradiated under the strongest brightness of 65.4 mW cm^{-2} (365 nm), 51.0 mW cm^{-2} (660 nm) and 135.4 mW cm^{-2} (450 nm), respectively. All the above light-adaptive memory behaviors were carried out in a 5 × 5 pixel array in the mimicking retina. All the light density values were the actual measured results based on the percentage adjustment of the respective LED power supply.

Cu/CFMPBI/Au indicates a diverse and promising application whenever in a dim or bright environment, in UV or visible radiation. What's more, Table S5 (Supporting Information) presents the state-of-the-art reported light-involved RS memristors. Among these various material systems, our work of Cu/CFMPBI/Au displays ultra-low V_{SET} (≈0.38 V) and a large on/off ratio (10^4) as well as good retention time (10^4 s). Besides, the light endurance of 600 cycles (Figure S19, Supporting Information) and broadband tunable multiple resistances (UV, Vis, White) also stand out. Besides, few works have simultaneously explored the photodetecting ability besides RS memory. Here, with the design of asymmetrical electrodes, the self-powered photoresponse is also achieved as well as sensing application. Importantly, due to the bi-phase cooperation in CFMPBI, the dual function of sensing and memory could be controlled depending on the applied voltage, which provides significant application scenarios.

Especially, in terms of memory, when compared to the binary in-situ memorization under darkness presented in Figure 1c, the light-dependent memory behavior can offer various tuning ranges for both '0′ and '1′, also as HRSs and LRSs, which gives the operated pixel with more light information. Although the 0/1 image possesses the advantages of high contrast and simplicity, a wide range of grayscale levels would be lost. While the light-adaptive memory could render much finer states to showcase multilevel light intensities. By gathering the R_{OFF}/R_{ON} among pixels, the ultimate images could be endowed with more details and depth variations, which provides great potential in achieving stereoscopic vision for complex scenes.

3. Conclusion

In summary, we have built a mimicking retina by RS photomemristors of $Cu/Cs_xFA_yMA_{1-x-y}Pb(I_zBr_{1-z})_3/Au$. The dual function was respectively demonstrated as photosensor and in-situ memorization. Specifically, the light sensing shows excellent self-powered, broadband (UV, Vis, NIR) photoresponse benefiting from the asymmetric electrode configuration. What's more, the visual adaptation processes are well imitated under dynamic light environments including photopic and scotopic imaging. After the light exposure is removed, the perceived image can be electrically memorized on the same device array, with a low power consumption of ≈100 pW for each write operation, exhibiting a small V_{th} of ≈0.38 V, a high on/off ratio of 10^4, and a long retention time of over 10^4 s. In addition, the light-adaptive memory is the first time demonstrated on the machine eye for broad wavelengths application (UV, Vis, White light), endowing the image more finer contrast information compared to binary image. As a result, our study gives a promising insight into high-performance RS-type photomemristors, as well as the mimicking retina application especially utilized in varied light scenarios.

Supporting Information

Supporting Information is available from the Wiley Online Library or from the author.

Acknowledgements

This work was supported by National Natural Science Foundation of China (No. 62374035, 92263106, and 12211530438) and Science and Technology Commission of Shanghai Municipality (No. 21520712600 and 19520744300).

Conflict of Interest

The authors declare no conflict of interest.

Data Availability Statement

The data that support the findings of this study are available from the corresponding author upon reasonable request.

Keywords

light-adaptive, mimicking retina, perovskite, RS photomemristor, self-powered

Received: March 17, 2024
Published online: May 3, 2024

[1] Y. Hou, J. Li, J. Yoon, A. M. Knoepfel, D. Yang, L. Zheng, T. Ye, S. Ghosh, S. Priya, K. Wang, *Sci. Adv.* **2023**, *9*, eade2338.
[2] J. Meng, T. Wang, H. Zhu, L. Ji, W. Bao, P. Zhou, L. Chen, Q. Sun, D. W. Zhang, *Nano Lett.* **2022**, *22*, 81.
[3] R. Yu, L. He, C. Gao, X. Zhang, E. Li, T. Guo, W. Li, H. Chen, *Nat. Commun.* **2022**, *13*, 7019.
[4] D. Lee, M. Park, Y. Baek, B. Bae, J. Heo, K. Lee, *Nat. Commun.* **2022**, *13*, 5223.
[5] W. Liu, X. Yang, Z. Wang, Y. Li, J. Li, Q. Feng, X. Xie, W. Xin, H. Xu, Y. Liu, *Light Sci Appl* **2023**, *12*, 180.
[6] S. M. Kwon, S. W. Cho, M. Kim, J. S. Heo, Y. Kim, S. K. Park, *Adv. Mater.* **2019**, *31*, 1906433.
[7] G. X. Zhang, Z. C. Zhang, X. D. Chen, L. Kang, Y. Li, F. D. Wang, L. Shi, K. Shi, Z. B. Liu, J. G. Tian, T. B. Lu, J. Zhang, *Sci. Adv.* **2023**, *9*, eadi5104.
[8] W. Chen, Z. Zhang, G. Liu, *iScience* **2022**, *25*, 103729.
[9] Y. Tan, H. Hao, Y. Chen, Y. Kang, T. Xu, C. Li, X. Xie, T. Jiang, *Adv. Mater.* **2022**, *34*, 2206816.
[10] X. Fu, T. Li, B. Cai, J. Miao, G. N. Panin, X. Ma, J. Wang, X. Jiang, Q. Li, Y. Dong, C. Hao, J. Sun, H. Xu, Q. Zhao, M. Xia, B. Song, F. Chen, X. Chen, W. Lu, W. Hu, *Light Sci Appl* **2023**, *12*, 39.
[11] X. Zhao, Z. Wang, W. Li, S. Sun, H. Xu, P. Zhou, *Adv. Funct. Mater.* **2020**, *30*, 1910151.
[12] D. J. Kim, Y. J. Tak, W.-G. Kim, J. K. Kim, J. H. Kim, H. J. Kim, *Adv. Mater. Interfaces* **2017**, *4*, 1601035.
[13] C. Hung, Y. Chiang, Y. Lin, Y. Chiu, W. Chen, *Adv. Sci.* **2021**, *8*, 2100742.
[14] X. Guan, W. Hu, M. A. Haque, N. Wei, Z. Liu, A. Chen, T. Wu, *Adv. Funct. Mater.* **2018**, *28*, 1704665.
[15] T. Paul, P. K. Sarkar, S. Maiti, K. K. Chattopadhyay, ACS Appl. Electron. Mater. **2020**, *2*, 11, 3667.
[16] X. Guan, Y. Wang, C. H. Lin, L. Hu, S. Ge, T. Wan, A. Younis, F. Li, Y. Cui, D. C. Qi, D. Chu, X. D. Chen, T. Wu, *Appl. Phys. Rev.* **2020**, *7*, 031401.
[17] N. Li, S. Zhang, Y. Peng, X. Li, Y. Zhang, C. He, G. Zhang, *Adv. Funct. Mater.* **2023**, *33*, 2305589.
[18] S. Y. Li, X. Y. Liu, H. Yang, H. Zhu, X. S. Fang, *Nat. Electron.* **2024**, *7*, 216.

[19] F. Cao, Z. Hu, T. Yan, E. Hong, X. Deng, L. Wu, X. S. Fang, *Adv. Mater.* **2023**, *35*, 2304550.
[20] H. Ye, Z. Liu, B. Sun, X. Zhang, T. Shi, G. Liao, *Adv. Electron. Mater.* **2023**, *9*, 2200657.
[21] Z. Wang, Z. Shi, T. Li, Y. Chen, W. Huang, *Angew. Chem., Int. Ed.* **2017**, *56*, 1190.
[22] X. Fu, S. Jiao, Y. Jiang, L. Li, X. Wang, C. Zhu, C. Ma, H. Zhao, Z. Xu, Y. Liu, W. Huang, W. Zheng, P. Fan, F. Jiang, D. Zhang, X. Zhu, X. Wang, A. Pan, *ACS Appl. Mater. Interfaces* **2020**, *12*, 2884.
[23] Y. Liu, Y. Liu, Y. Guo, *Mater. Chem. Front.* **2023**, *7*, 5215.
[24] Y. Zhang, S. Poddar, H. Huang, L. Gu, Q. Zhang, Y. Zhou, S. Yan, S. Zhang, Z. Song, B. Huang, G. Shen, Z. Fan, *Sci. Adv.* **2021**, *7*, eabg3788.
[25] B. Hwang, J. S. Lee, *Adv. Electron. Mater.* **2019**, *5*, 1800519.
[26] Wang, Z. Z., Y. Xiong, X. Dong, J. Sha, X. Bai, W. Li, Y. Yin, Y. Wang, *Nanotechnology* **2021**, *32*, 375201.
[27] F. Zhou, Y. Liu, X. Shen, M. Wang, F. Yuan, Y. Chai, F. Zhou, Y. Liu, X. Shen, M. Wang, F. Yuan, Y. Chai, *Adv. Funct. Mater.* **2018**, *28*, 1800080.
[28] J. Han, X. Shan, Y. Lin, Y. Tao, X. Zhao, Z. Wang, H. Xu, Y. Liu, *Small* **2023**, *19*, 2207928.
[29] J. L. de Bougrenet de la Tocnaye, *C R Biol* **2022**, *345*, 135.
[30] H. M. Mohammadi, M. H. Edrisi, Y. Savaria, *IEEE Access* **2023**, *11*, 80020.
[31] P. Werginz, B. Y. Wang, Z. C. Chen, D. Palanker, *J Neural Eng* **2020**, *17*, 045008.
[32] M. Wang, J. Liu, C. Ma, Y. Wang, J. Li, J. Bian, *J. Electron. Mater.* **2022**, *51*, 2381.
[33] J. Yu, B. Huang, X. Zheng, H. Wang, F. Chen, S. Xie, Q. Wang, J. Li, *Small* **2022**, *18*, 2200523.
[34] F. Xu, T. Zhang, G. Li, Y. Zhao, *J. Mater. Chem. A* **2017**, *5*, 11450.
[35] G. Murugadoss, P. Arunachalam, S. K. Panda, M. Rajesh Kumar, J. R. Rajabathar, H. Al-Lohedan, M. D. Wasmiah, *J Mater Res Technol* **2021**, *12*, 1924.
[36] S. Zhan, Y. Duan, Z. Liu, L. Yang, K. He, Y. Che, W. Zhao, Y. Han, S. Yang, G. Zhao, N. Yuan, J. Ding, S. (Frank), *Adv. Energy Mater.* **2022**, *12*, 2200867.
[37] J. X. Zhong, J. F. Liao, Y. Jiang, L. Wang, D. Bin Kuang, W. Q. Wu, *J. Mater. Chem. A* **2020**, *8*, 9743.
[38] J.-M. Yang, S.-G. Kim, J.-Y. Seo, C. Cuhadar, D.-Y. Son, D. Lee, N.-G. Park, *Adv. Electron. Mater.* **2018**, *4*, 1800190.
[39] J. Luo, Z. Zhao, X. Huang, Y. Wu, Z. Liu, A. Wei, J. Liu, Y. Zhao, Z. Xiao, X. Yang, *Mater. Today Commun.* **2022**, *33*, 104186.
[40] B. Slimi, M. Mollar, I. Ben Assaker, I. Kriaa, R. Chtourou, B. Marí, *Energy Procedia* **2016**, *102*, 87.
[41] F. Liao, Z. Zhou, B. J. Kim, J. Chen, J. Wang, T. Wan, Y. Zhou, A. T. Hoang, C. Wang, J. Kang, J. H. Ahn, Y. Chai, *Nat. Electron.* **2022**, *5*, 84.